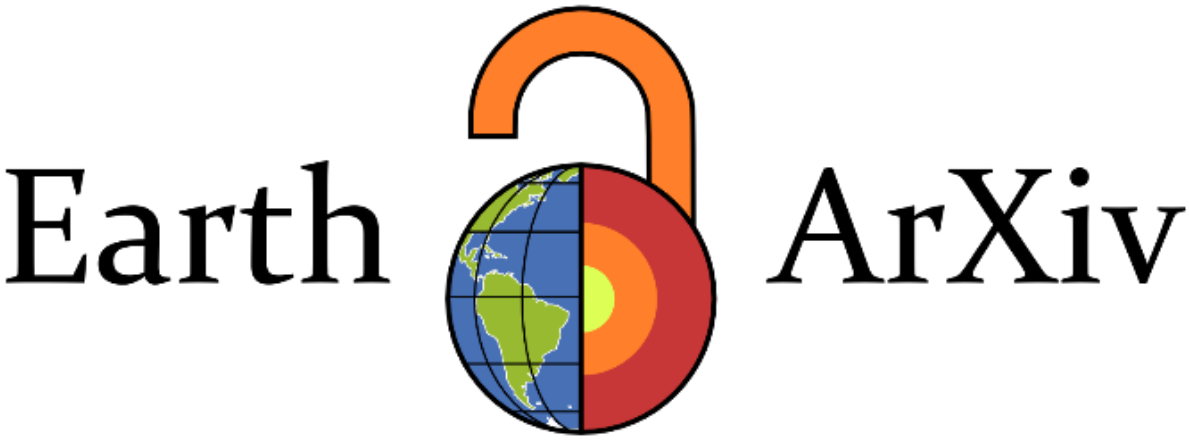

Constraints on magma source conditions from hydraulic fracture models and seismic observations of dyke tip deceleration

Timothy Davis[1], and Juliet Biggs[1].

[1]COMET, School of Earth Sciences, University of Bristol, UK

Key Points:

- Seismicity shows lateral dykes decelerate as they propagate and the tip speed decays as the inverse square root of time
- We use hydraulic fracture theory to show that lateral dykes decelerate following a power law set by the source condition
- The observed deceleration is consistent with near-constant source pressure but not constant flux or volume conditions

Corresponding author: Timothy Davis, timothy.davis@bristol.ac.uk

Abstract

Seismicity shows that magmatic dykes decelerate as they propagate laterally. Hydraulic fracture theory shows this deceleration relates to the coupling between the source and the dyke. Here, we use hydraulic fracture models to derive scaling laws for the length, width, and shape of dykes driven by three source boundary conditions: constant flux, constant pressure, and a finite volume release. These span end-member source behaviours: a stiff source supplying steady flux regardless of dyke pressure, a compliant reservoir in pressure equilibrium whose supply decays with time, and an instantaneous release representing rapid exhaustion of the supply. Denoting dyke length and height as L and H respectively, we obtain analytical solutions for two end-member geometries: an early, vertically tall fracture ($L < H$) that transitions to a laterally long, vertically short one ($L > H$) as the dyke propagates. While $L/H \ll 1$ the constant-pressure condition yields exponential growth in length, but once $L > H$ constant flux gives $L \propto t^{4/5}$, constant source pressure gives $L \propto t^{1/2}$, and a finite volume release gives $L \propto t^{1/5}$. Comparing these predictions to six lateral dyking episodes with $L < 25$ km, we find the seismicity fronts consistently follow $L \propto t^{1/2}$, indicating that dykes are driven by a near-constant source pressure. A well-constrained source condition is a prerequisite for any model that probes the dynamics of dyke intrusions, including the mechanisms of arrest and start-stop behaviour. Thus, hydraulic fracture models offer a framework for forecasting the temporal evolution of dyke propagation.

Plain Language Summary

Dykes are large magma-filled cracks that intrude beneath the Earth's surface. Lateral dykes can propagate sideways away from volcanic centres threatening nearby populations with a range of hazards. Such cracks can extend up to 50 kilometres away from their source, be a number of kilometres high and 1 to 10 metres wide. As they intrude sideways into the surrounding rock they cause tiny earthquakes. Tracking of the earthquakes shows the dyke velocity slows with time. Theory from the hydraulic fracturing literature shows that the rate at which the intrusion decelerates is related to the way in which the magma source feeds the dyke. Comparing theory to data, we show that the source maintains a near constant pressure whilst draining to feed the dyke. This may be due to a number of processes that can keep the source pressure high even as fluid drains into the dyke. Understanding how the source drains into the dyke means we may be able to forecast not just the path a dyke takes, but how its speed changes as it propagates.

1 Introduction

Lateral dyke intrusions are three-dimensional magma-filled fractures that propagate horizontally through the Earth's crust, posing significant hazards to local populations. Since 2020, four major lateral dyking events have forced the evacuation of at least 10,000 people (OCHA, 2020; Bato et al., 2021; Smittarello et al., 2022; OCHA, 2021; Lewi et al., 2025; EMSC, 2025). Recent advances in physically-grounded kinematic inversions have provided high temporal resolution insights into the changing dyke geometries as these propagate laterally (e.g., Heimisson & Segall, 2020; Lomax et al., 2025). These reconstruct geometry from elastic deformation but treat each time step independently — without using the physics of fluid flow to link successive solutions, the implied magma transport between steps is not guaranteed to be physically realistic. Capturing that flow requires modelling the physical process directly, which for lateral dyking in three dimensions remains challenging (Rivalta et al., 2015; Zia & Lecampion, 2020). At a minimum, such models must capture the forcing that drives fluid into the fracture, the fluid flow within the dyke, elastic deformation of the surrounding medium, and fracture propagation at the crack tip. As yet, no studies have compared the differing predictions of such

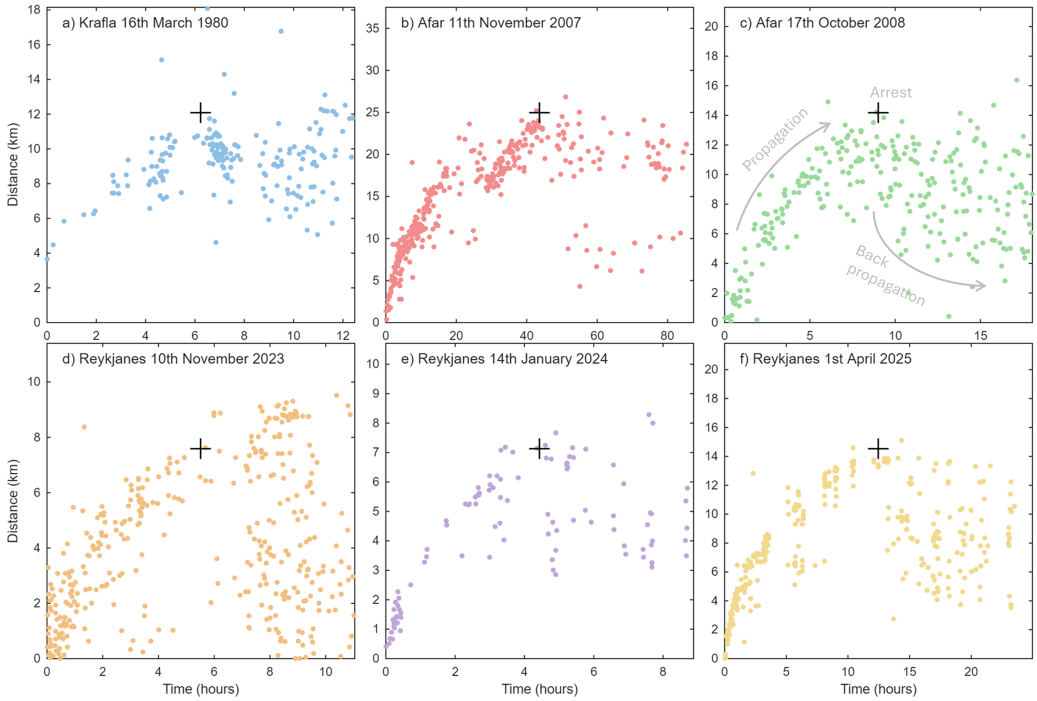

Figure 1. Spatio-temporal patterns of seismicity for six different dyke intrusions. **Panel a** Krafla in NE Iceland from (Brandsdóttir & Einarsson, 1979). **Panels b–c** Afar dykes from (Belachew et al., 2011) and **Panels d–f** Dykes from the Reykjanes peninsula in SW Iceland from the Icelandic Meteorological Office catalogue. Arrest length and time shown as a black cross.

coupled models against observational constraints and it remains unclear how sensitive the models are to the choice of forcing or the assumed dyke geometry.

Seismic observations show the velocity of a propagating dyke tip decreases with time (Brandsdóttir & Einarsson, 1979; Einarsson & Brandsdóttir, 2021) and geodetic inversions show decreasing rates of both dyke and source volume change (Rivalta, 2010; Sigmundsson et al., 2024). In Figure 1 we show example seismic records from six lateral dyking events over the last 50 years from Iceland and Ethiopia (Brandsdóttir & Einarsson, 1979; Belachew et al., 2011). Despite the differing lengths and distances at which these arrest, all intrusions show a similar pattern with a decreasing rate of propagation with time, followed by arrest and back-propagation of seismicity. Here, we focus on dykes with lengths below 25 km; larger dykes in the presence of topography are often segmented, with patterns of arrest and renewed propagation that interrupt the smoothly decaying front speed (Ágústsdóttir et al., 2016; Lengliné et al., 2021; Smittarello et al., 2022; Isken et al., 2025). These seismic records provide a rich dataset for testing models of propagating fluid-filled fractures from magmatic and hydraulic fracturing literature.

Previous studies of magmatic systems have coupled dykes to magma chambers, suggesting the deceleration of the dyke front is related to the magma chamber depressurisation (Rivalta, 2010; Grossman-Ponemon et al., 2020). In this study, we use height-constrained models from the hydraulic fracturing literature to study lateral dyke propagation, comparing the predicted scaling laws to seismic datasets (Perkins & Kern, 1961; Nordgren, 1972). We build on the work of Lister and Kerr (1991) and A. P. Bunger et al. (2013) who used similar models to show that magmatic dykes will decelerate due to elastic-fluid

coupling alone. We explore how the speed of the propagating dyke scales depending on the source boundary conditions and compare the influence of differing boundary conditions on the geometry during propagation. We test when 2D plane strain models and the simplified elasticity assumptions of 3D height-constrained models in the hydraulic fracturing literature are appropriate. We do this by exploring the effect of intermediate geometries, accounting for the full 3D elastic effects and comparing to end member predictions. Finally, we compare our results to seismic observations to understand the forcing driving magmatic dyke intrusions laterally.

2 Governing equations

Hydraulic fracture models are governed by the coupling between elastic deformation of the host rock and viscous fluid flow within the fracture, and the form of this coupling depends strongly on the assumed geometry. Full 3D and pseudo-3D approaches allow fracture height to vary but require assumptions about the nature of the crust trapping the dyke (Lister & Kerr, 1991; Bolchover & Lister, 1999; Möri et al., 2023; Davis et al., 2026).

We consider a hydraulic fracture propagating in an infinite impermeable elastic medium. The fluid inside the fracture is an incompressible Newtonian fluid. The problem is governed by the coupling between solid mechanics (elastic deformation) and fluid mechanics (viscous flow). Assuming laminar incompressible flow in the x direction through a slot aligned in x and with a wall separation w in y Poiseuille's law is

$$q = -\frac{w^3}{\mu'}\frac{\partial p}{\partial x}. \tag{1}$$

where μ is the dynamic fluid viscosity and $\mu' = 12\mu$ and p is the fluid pressure. The Reynolds equation that governs the flow of fluid in the fracture is given by

$$\frac{\partial w}{\partial t} = -\frac{\partial q}{\partial x} = \frac{1}{\mu'}\frac{\partial}{\partial x}\left(w^3\frac{\partial p}{\partial x}\right), \tag{2}$$

where the two-dimensional flux is q.

2.1 Simplified model geometries and key scales

Figure 2 illustrates the two simplified model geometries used in this study: a vertically-elongated fracture representing the early stages of lateral dyke propagation ($L < H$) and a laterally elongated fracture representing the dyke once its length becomes greater than its height ($L > H$). The two geometries can be visualised by comparison to well-known pasta shapes: lasagna is an example of early-stage vertically-elongated geometry and linguine is an example of laterally-elongated late-stage geometry. For both geometries, it is possible to simplify the equations relating the internal fluid pressure to the fracture wall opening (Perkins & Kern, 1961; Khristianovic & Zheltov, 1955; Geertsma & De Klerk, 1969).

Figure 2a shows a vertically-elongated dyke where $L/H \ll 1$ and the dyke is far taller than it is long. In the hydraulic fracturing literature this is known as a Khristianovich–Geertsma–de Klerk (KGD) geometry (Khristianovic & Zheltov, 1955; Geertsma & De Klerk, 1969). In this model geometry, the height is infinite in the z direction and every horizontal slice through the fracture has the same width distribution. There is no strain in the z-direction resulting in a state of plane strain in the propagation plane. The opening at any point therefore depends on the entire distribution of pressure along x, coupled through an elastic integral equation. Pressure and width are connected; changing the pressure at one location in x alters the width distribution of the whole fracture. This geometry is appropriate when the dyke length is smaller than its height, for example during the early stages of lateral propagation before the dyke has grown much beyond its vertical extent.

A simpler and well-validated alternative is to treat the fracture as height-constrained with an elliptical cross-sectional profile whose width varies along the fracture length. We refer to fixed-height geometries as any model with vertical extent H and with yz cross-sections of an elliptical form. We refer to models where a simplified elasticity relation is used in each yz cross-section as Perkins–Kern–Nordgren (PKN) models (Perkins & Kern, 1961; Nordgren, 1972). PKN models have previously been applied to model lateral dyke propagation (A. P. Bunger et al., 2013). Figure 2b shows the fixed-height geometry where $L/H \gg 1$ and the dyke is vertically short and laterally long. Provided the fracture has a large length-to-height ratio ($L/H \gg 1$), this means that each vertical cross-section deforms as though it were elastically independent of its neighbours. The width profile at a given x is set entirely by the local fluid pressure $p(x)$ and the fixed height H, with no integral coupling along x. This is the local-elasticity approximation. Because neighbouring sections do not communicate elastically, the model cannot resolve large along-fracture pressure gradients; it is accurate only when pressure varies slowly over length-scales comparable to H. The payoff is that a single continuity equation in x captures both elastic and viscous effects without a separate integral equation.

The modelling of fixed-height fractures has several advantages. Firstly, the length scaling of fractures whose height is regulated by various mechanisms is approximately equal to that of a fixed-height fracture (Nordgren, 1972; A. P. Bunger et al., 2013). Lister and Kerr (1991) show this for fractures trapped by crustal density gradients, Adachi et al. (2010) for fractures confined by elevated stresses in vertically stratified layers above and below, and Peruzzo and Lecampion (2026) for fractures confined between layers of greater fracture toughness. Thus, the model captures the first order effects dictating the lateral propagation speed and shape but does not require poorly constrained parameters that trap the dyke vertically. Secondly, efficient methods exist to model fractures with a fixed-height geometry. One dimensional elastic integrals allow for the incorporation of elastic effects in 3D without requiring highly complex 3D solvers such that existing PKN approximations can be tested (Adachi & Peirce, 2008; Dontsov & Peirce, 2016). Finally, there is a large amount of existing hydraulic fracturing literature modelling height constrained fractures driven by a constant flux allowing us to interpret our results and inspect our model assumptions more robustly. For example, hydraulic fracturing literature has covered topics such as the dominant energy sink in a height contained fracture and the influence of fluid leak-off which is akin to high rates of magma solidification (Kovalyshen & Detournay, 2010; Dontsov & Peirce, 2016).

2.1.1 Vertically-elongated (KGD) geometry

When the fracture is short in x relative to z then plane-strain conditions apply (Fig.2). Here (2) is used to model flow and the relationship between pressure and aperture is

$$p(s,t) = -\frac{E'}{4\pi L}\int_{-1}^{1}\frac{\partial w}{\partial s'}\frac{1}{s'-s}ds', \tag{3}$$

where $E' = E/(1-\nu^2)$(Peirce & Detournay, 2022). This elasticity kernel is non-local: the opening at any point depends on the loading distribution over the entire crack.

To extract the dominant length-dependence, we replace each quantity in (3) with its characteristic scale. The integration variable s' runs over $[-1,1]$ and $\partial w/\partial s'$ scales simply as w. The remaining integral $\int_{-1}^{1} ds'/(s'-s)$ is a dimensionless number of order unity. We therefore obtain

$$p \sim \frac{E'\,w}{L}. \tag{4}$$

This captures the essential feature driving the propagation dynamics: w scales linearly with the crack half-length L at fixed driving pressure. This scaling is meaningful because the dimensionless integral depends on geometry only, not on length or time, so it does not affect the scaling relations governing propagation. We show later that, under KGD

conditions with power-law (or constant) pressure forcing, the system admits self-similar solutions, so the rescaled profile $\Omega(\xi)$ collapses onto a single time-independent shape and the integral in (3) reduces to a fixed numerical constant.

2.1.2 Laterally-elongated fixed-height models

In our 3D fixed-height model (Fi g.2b) the width w is assumed elliptical in z

$$w(x,z,t) = w(x,0,t)\sqrt{1-\left(\frac{2z}{H}\right)^2}, \tag{5}$$

where the average cross-sectional width $\bar{w}$ is

$$\frac{\pi}{4}w(x,0,t) = \bar{w}(x,t) = \frac{1}{H}\int_{-H/2}^{H/2} w\partial z. \tag{6}$$

This analytical form can be combined with (1) to provide a modified Reynolds equation that provides the average flux over each elliptical cross-section

$$\frac{\partial \bar{w}}{\partial t} = -\frac{\partial \bar{q}}{\partial x} = \frac{1}{\bar{\mu}}\frac{\partial}{\partial x}\left(\bar{w}^3\frac{\partial p}{\partial x}\right), \tag{7}$$

where $\bar{q}$ is the average flow rate per unit fracture height and $\bar{\mu} = \pi^2\mu$, the flux is

$$\bar{q} = -\frac{\bar{w}^3}{\bar{\mu}}\frac{\partial p}{\partial x}. \tag{8}$$

This requires coupling to elasticity to compute the pressure gradient inside the fracture. The hyper-singular integral equation relating aperture to net pressure on the walls of a planar rectangular fracture can be reduced to a 1-D integral equation provided the fracture has the yz cross-sectional form of (5) (Adachi & Peirce, 2008; Dontsov & Peirce, 2016; Peirce, 2025). This captures the elastic effects in both x and z for a given average aperture distribution in x, providing the internal pressure inside the fracture, gradients of which drive flow

$$p(x,t) = \frac{\bar{E}}{\pi H}\int_{-L}^{L}\bar{w}(x',t)\frac{\mathrm{d}G(2(x'-x)/H)}{\mathrm{d}x'}\mathrm{d}x', \tag{9}$$

$$G(s) = \frac{\sqrt{1+s^2}}{s}E\left(\frac{1}{1+s^2}\right), \tag{10}$$

$$E(m) = \int_0^{\pi/2}\sqrt{1-m\sin^2\theta}\,\mathrm{d}\theta, \tag{11}$$

where G is a kernel that encodes the non-local elastic coupling, $E(m)$ is the complete elliptic integral of the second kind. This is coupled with Eq.(7) to model flow and the changing width of the fracture. Note, L in this equation is the length of one wing of the bi-directional fracture.

2.1.3 Local elasticity (PKN) geometry

Assuming $L \gg H$ the elastic integral in (9) reduces to a much simpler analytical form in each cross-section (Adachi & Peirce, 2008; Peirce, 2025). A straight fracture of length H loaded by a constant pressure p with the width distribution in (5) has an average width that is related to the internal pressure by

$$\bar{w} = \frac{Hp}{\bar{E}}. \tag{12}$$

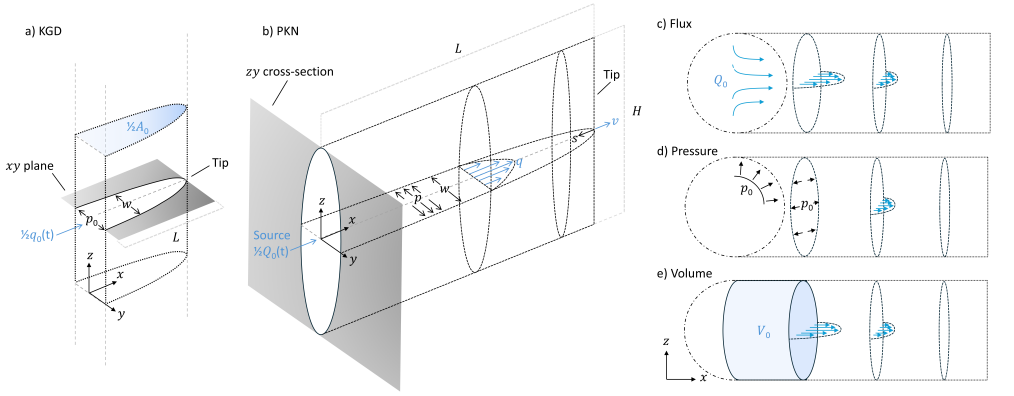

Figure 2. Comparison of the end member fracture shapes in this study. **Panel a** plane strain Kristianovich-Geertsma-de Klerk fracture model where $L/H \ll 1$ and both shape and flow speed are uniform in z. **Panel b** long, vertically short fixed-height fracture known as the Perkins-Kern and Nordgren geometry where $L/H \gg 1$. Here the height is fixed in z and each $y-z$ cross-section is elliptical. The right hand schematics compare the different forcing conditions. **Panel c** represents a constant flux, **Panel d** a constant pressure and **Panel e** a constant volume.

In the PKN geometry this analytical relation between pressure and width is treated as independent in each cross-section of the fracture, with no pressure dependence on the changing width in x. To keep our equations uncluttered we introduce the following constants

$$\begin{aligned} \mu' &= 12\mu, \quad \bar{\mu} = \pi^2\mu, \\ E' &= \frac{E}{1-\nu^2}, \quad \bar{E} = \frac{2}{\pi}E', \\ K' &= \frac{8}{(2\pi)^{1/2}}K_I, \quad \bar{K} = \left(\frac{8}{\pi}\right)^{1/2}K_c, \end{aligned} \tag{13}$$

where E is the Young's Modulus, ν the Poisson's ratio and K_c the mode one fracture toughness (Kovalyshen & Detournay, 2010; Dontsov & Peirce, 2016; Peirce, 2025). Substituting the elastic response (12) into the Poiseuille's law results in

$$\bar{q} = -\frac{\bar{w}^3}{\bar{\mu}}\frac{\partial}{\partial x}\left(\frac{\bar{E}}{H}\bar{w}\right) = -\frac{\bar{E}}{4\bar{\mu}H}\frac{\partial \bar{w}^4}{\partial x}, \tag{14}$$

such that the mass conservation equation becomes a single, fully-coupled partial differential equation

$$\frac{\partial \bar{w}}{\partial t} = -\frac{\partial \bar{q}}{\partial x} = \frac{\bar{E}}{4\bar{\mu}H}\frac{\partial^2 \bar{w}^4}{\partial x^2}. \tag{15}$$

This is a non-linear advection-diffusion equation for the fracture width w. This equation resembles the heat equation, relating the curvature of $\bar{w}^4$ in x to the change in average width $\bar{w}$ with time. We test the validity of this assumption later using the non-local elastic relation (9).

2.2 Boundary conditions

Closure of the system requires two boundary conditions: the source condition at $x = 0$ and the propagation condition at the fracture tip $x = L(t)$. Exploiting the symmetry of the fracture about $x = 0$, we solve on the half-domain $0 \le x \le L(t)$ and impose boundary conditions at each end. At $x = 0$, the source condition represents the magma reservoir feeding the dyke (Fig.2). At $x = L(t)$, the tip condition applies at the moving propagation front.

2.2.1 Source boundary conditions

We consider three source boundary conditions driving the fracture laterally: constant flux, constant pressure and a constant volume (Fig.2c–e). Constant flux represents a stiff source that maintains a steady supply irrespective of the dyke's resistance; constant pressure represents a compliant reservoir that equilibrates with the dyke such that the flux decays with time; and constant volume represents a finite pulse of magma injected near-instantaneously after which the source is exhausted and the dyke propagates on its stored fluid alone.

For an impermeable medium with no leak-off, global volume balance requires that the injected volume equals the fluid stored in the fracture. The source flux condition and volume balance for a KGD and fixed-height 3D fracture are

$$\frac{\mathcal{Q}_0(t)}{2\,H^{\,k}} = -\frac{1}{\mu'}\left(\frac{\mu'}{\bar{\mu}}\right)^{k}\left(\frac{\pi}{4}\right)^{3k} w_c^{\,3}\,\frac{\partial p}{\partial x}\bigg|_{x=0^+}, \tag{16}$$

$$2\left(\frac{\pi}{4}\right)^{k}\int_0^{L(t)} w_c(x,t)\,\mathrm{d}x = \frac{\mathcal{V}(t)}{H^{\,k}}, \tag{17}$$

where $w_c(x,t) = w(x,0,t)$ is the centre width, and $k = 0$ recovers the KGD fracture while $k = 1$ gives the fixed-height fracture. Here $\mathcal{V}$ is the fracture cross-sectional area (KGD) or volume (fixed-height), and $\mathcal{Q}_0$ is the source flux into the fracture (2D or 3D flux respectively); (16) sets the flux at the source $x = 0^+$ and (17) enforces global volume balance.

2.2.2 Fracture tip

The tip region of a hydraulic fracture is where the majority of energy is dissipated. Two mechanisms contribute to energy dissipation at the tip: viscous dissipation, which becomes large near the tip as the aperture tapers to zero and fluid is forced through a vanishingly small gap, and fracture energy, expended in breaking the rock ahead of the advancing tip. The balance between these two sinks defines the viscous- and toughness-dominated propagation regimes; we assume the fracture is propagating in the viscous regime for the remainder of the analysis. Asymptotic scaling has been used to define how the fracture width relates to the distance from the fracture tip as it is approached (Detournay, 2016). At the fracture tip ($x = L(t)$), the following boundary condition is imposed

$$w = 0, \quad q = 0 \quad \text{at} \quad x = \pm L(t), \tag{18}$$

which assumes the fluid is coincident with the fracture tip. Supposing

$$s = L - x, \tag{19}$$

for a fixed height 3D fracture where toughness is zero, the resulting tip asymptote takes the form

$$\bar{w}_m(s) = 3^{5/6}\left(\frac{\bar{\mu}v}{\bar{E}}\right)^{1/3} s^{2/3}, \qquad \frac{s}{L} \ll 1. \tag{20}$$

This follows the proof of transformation from viscosity dominated plane strain asymptote to a fixed-height geometry in Peirce (2025). Models that use local PKN elasticity (12) have issues when $s/H < 1$, Kovalyshen and Detournay (2010) provide an adjusted asymptote for this specific case. When toughness is non-negligible, the fracture shape at the tip takes the form

$$\bar{w}_k = \frac{\bar{K}}{\bar{E}} s^{1/2}. \tag{21}$$

For any non-zero fracture toughness, the toughness asymptote always applies in a region close to the tip. However, when viscous dissipation dominates, this toughness-controlled region becomes vanishingly small (A. Bunger et al., 2007). In the Supporting Information, we show lateral dykes typically propagate in a viscosity dominated regime.

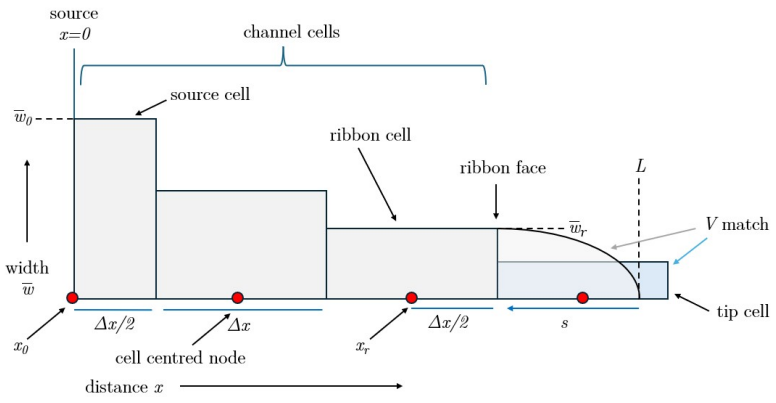

Figure 3. Numerical setup of the grid. Cell centres shown as red dots, the discrete widths along the y axis. The tip cell volume matches the volume of the curved asymptotic profile shown. s is the distance measured from the tip.

3 Numerical model

3.1 Numerics

The governing equations are solved on a fixed, uniform grid with spacing Δx using finite-difference and finite-volume methods with an explicit, adaptive time-stepping scheme. We exploit the symmetry of the problem and model only the half-domain $x \geq 0$. Fig. 3 shows the geometry and different cells. At each cell centre, the pressure is obtained from the current width distribution using the elasticity relation appropriate to the geometry (Eqs. (9), (3) or (12)). The continuity equation ((2) or (7)) then governs the evolution of width given this pressure field; closure of the system requires the use of the two boundary conditions.

At $x = 0$ the source boundary condition is imposed as follows. For constant flux and fixed volume, the source-cell flux is set to the prescribed injection rate or to zero, respectively. For constant pressure we solve for a new source-cell width such that the prescribed pressure p_0 here is met; the flux from this cell then follows from the updated width and pressure gradient.

At the fracture tip, the moving front is tracked using the Implicit Level Set Algorithm (ILSA) (Peirce & Detournay, 2008). This algorithm prescribes the tip asymptotic in a weak sense: the width of the penultimate cell (ribbon), together with the applicable tip asymptote, is used to estimate the fracture front location. The tip cell width is set by matching this to the asymptote volume integral to the ribbon face. The front position, channel and tip widths are adjusted iteratively until all are consistent with the tip asymptote. The width of the tip cell is prescribed as the integral of this asymptote to the ribbon face, divided by Δx (Fig. 3).

3.2 End member solutions

Figure 4 shows numerical simulations of the width change when driven by the three boundary conditions and the two different geometries we consider; vertically-elongated KGD fractures and laterally-elongated PKN fractures. Fracture toughness is set to zero in these simulations. The profiles illustrate the key features that we will explain in the scaling analysis of Section 4. For both KGD and PKN fractures driven by a constant flux, fluid is supplied at a steady rate so the fracture volume grows linearly with time (Fig.4a,d). The source width increases as fluid accumulates faster than it can be transported to the

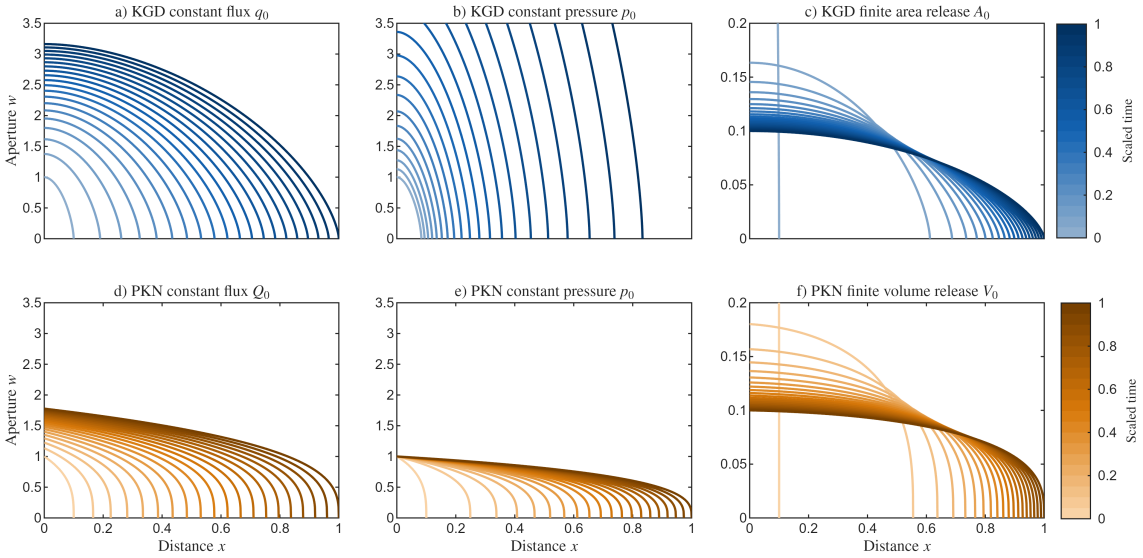

Figure 4. The shape evolution of hydraulic fractures under three forcing conditions. **Panels a-–c** show KGD fractures driven by constant flux, pressure, and area forcing, respectively; **Panels d-–f** show equivalent PKN results. Widths are normalized by their initial value, distance by the final fracture length, and time by the simulation end time. Note that panels c and f (finite area and volume-driven cases) use a different y-axis range, reflecting rapidly decreasing fracture widths under this forcing.

tip, and the fracture lengthens progressively with profiles that are roughly evenly spaced in time.

Under constant pressure, initially, while the dyke is vertically-elongated, the KGD fracture must widen to maintain the source pressure condition; this results in increasingly spaced profiles as the fracture tip accelerates due to an ever increasing flux. For the PKN fracture the source width of the fracture is fixed, set directly by the imposed pressure through the local elasticity relation. Because the pressure gradient between source and tip diminishes as the fracture lengthens, the flux into the fracture decays with time. The fracture still lengthens, but at an ever-decreasing rate, and the profiles become increasingly bunched at later times as the tip velocity drops.

Under a finite volume release, the fracture contains a fixed quantity of fluid that must redistribute under its own elastic pressure gradients. For both KGD and PKN fractures, as these lengthen, conservation of volume demands that the width must decrease as the fluid spreads and thins. The source width drops rapidly at early times when aperture gradients are large, then decays more slowly as the profile flattens. Here the lateral bunching of successive profiles at later times is especially pronounced.

3.3 Full numerical solution

We use the numerical solution incorporating non-local elasticity to test how vertically-elongated (KGD) fractures transition to laterally-elongated (PKN) fractures under different forcings. Using a fixed-height numerical model we employ the non-local elasticity integral (9). We model the fracture propagating across the domain, starting with a horizontally short, vertically elongated fracture of length-to-height ratio $L/H = 0.01$.

Fig. 5 shows the scaled fracture length L/H as a function of scaled time. Tip velocities correspond to the slope of the line, and these increase exponentially at early times, followed by a transition to a power-law scaling that shows as a straight line on the graph. In the following sections we derive analytical predictions of the two end-members and discuss the transition between these.

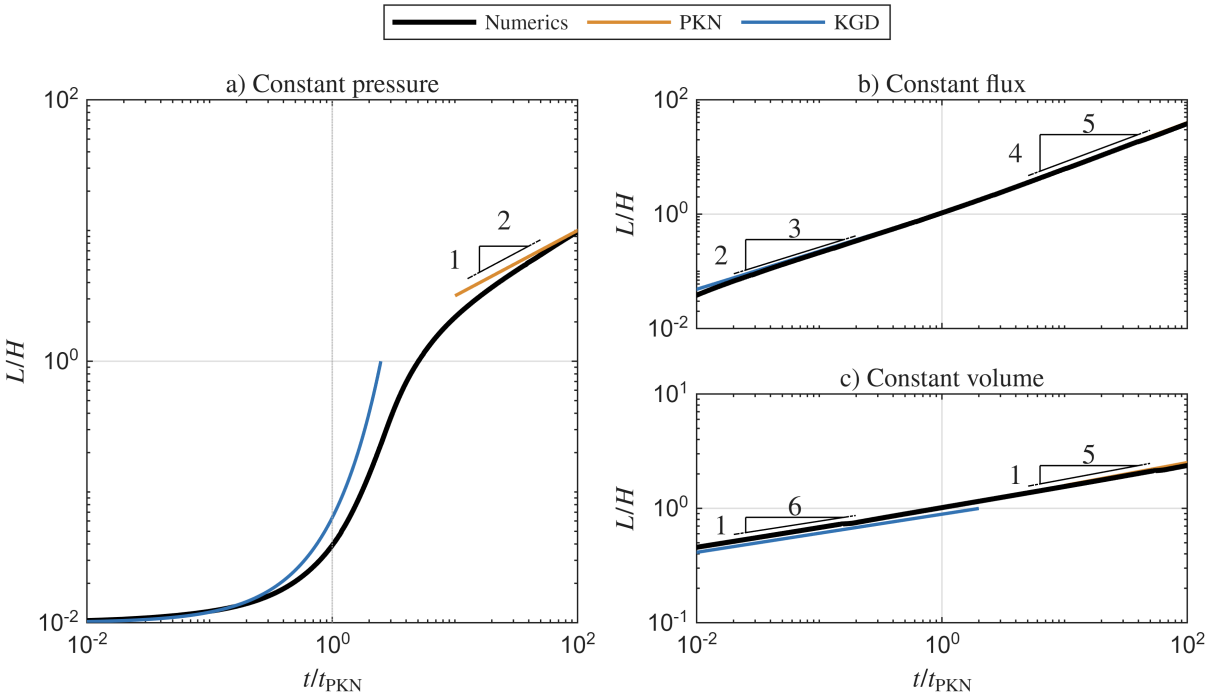

Figure 5. Fracture length change when non-local elasticity is considered. The numerical results capture the transition from the KGD to the PKN scaling. Panels compare the forcing. **Panel a** constant source pressure. **Panel b** Constant flux and **Panel c** constant volume. Analytical predictions for KGD and PKN speed are from Table.1. Times are scaled by $t_{\mathrm{PKN}}(L = H)$ which is the time taken for the PKN analytical prediction for that source condition to propagate length H.

4 Scaling laws

4.1 Deceleration of front propagation speed

We now detail characteristic scaling relations for laterally propagating dykes using the governing PDE and mass conservation, following the approach of Lister and Kerr (1991, sec. 5.4) and A. P. Bunger et al. (2013). We assume power-law scalings $V \sim t^{\alpha}$, $L \sim t^{\beta}$ and $w \sim t^{\gamma}$ and compare the results for our three different boundary conditions and our two end-member fracture geometries.

4.1.1 Scaling relations for KGD ($L \ll H$) geometry

The scaling for a KGD fracture with a constant flux has been previously provided in Detournay (2004) and D. I. Garagash (2006). Here we extend this analysis to cover constant pressure and constant volume boundary conditions.

The flow in the fracture is governed by the lubrication (Reynolds) equation (2). For a plane-strain crack of half-length L, the characteristic opening scales as (4). Width and length are elastically coupled: a longer crack will open more when subject to the same pressure.

The pressure inside the fracture scales as $p \sim E'w/L$ and assuming p scales with L, $\partial p/\partial x \sim E'w/L^2$. The lubrication equation (2) in scaling form becomes

$$\frac{w}{t} \sim \frac{E'}{\mu'}\frac{w^4}{L^3}, \tag{22}$$

We assume power-law scalings $L \sim t^\beta$ and $w \sim t^\gamma$. Balancing exponents gives

$$\gamma - 1 = 4\gamma - 3\beta \quad \Longrightarrow \quad 3\beta = 3\gamma + 1. \tag{23}$$

while mass conservation ($A \sim wL \sim t^\alpha$) gives

$$\gamma + \beta = \alpha. \tag{24}$$

Solving simultaneously:

$$\gamma = \frac{3\alpha - 1}{6}, \quad \beta = \frac{3\alpha + 1}{6}. \tag{25}$$

For the constant-flux ($\alpha = 1$) and finite-volume ($\alpha = 0$) cases, the general scaling relations yield well-defined power-law solutions. Substituting the source condition into the PDE balance and mass conservation gives the full dimensional scalings summarised in Table 1 with $L \sim t^{2/3}$ for constant flux and $L \sim t^{1/6}$ for a finite area release.

However, the application of a constant source pressure boundary condition is incompatible with power-law growth in the KGD geometry. Applying our power-law scaling analysis to the plane-strain elasticity relation (3) gives $p \sim E'w/L \sim t^{\gamma-\beta} = t^{-1/3}$, so the source pressure always decays as the crack lengthens regardless of source boundary condition.

4.1.2 Constant source pressure for KGD geometry: exponential growth

To find the growth law for constant source pressure in KGD geometry, we balance the lubrication flux against the rate of volume change directly. The flux scales as $q \sim w^3 p_0/(\mu' L) \sim L^2 p_0^4/(\mu' E'^3)$, while the rate of volume change is $dA/dt \sim (p_0/E')L\,dL/dt$. Equating these gives

$$\frac{dL}{dt} \sim \frac{L p_0^3}{\mu' E'^2}, \tag{26}$$

which is a linear ODE in L with the solution

$$L(t) = L_0 \exp\left(C_P \frac{p_0^3}{\mu' E'^2} t\right), \tag{27}$$

where C_P is a numerical constant and L_0 is the initial crack length. The width and velocity grow in proportion to L:

$$w(t) = \frac{p_0}{E'} L(t), \qquad v(t) = C_P \frac{p_0^3}{\mu' E'^2} L(t). \tag{28}$$

The exponential growth arises because the positive feedback between length and width is unrestrained: a longer crack is wider, which reduces the viscous resistance to flow, which drives faster lengthening, which opens the crack further. In practice, exponential growth cannot persist indefinitely: as the crack lengthens it will transition to the constant pressure PKN regime (once $L \gg H$), when the source pressure drops due to depletion, or when other dissipative processes (e.g. leak-off, solidification) become significant. The exponential regime is thus expected to characterise an early, transient phase of propagation.

4.1.3 Scaling relations for PKN ($L \gg H$) geometry

The length to time scaling for a PKN fracture has previously been derived for a constant flux in Nordgren (1972); Kemp (1990); Kovalyshen and Detournay (2010), for a constant pressure in A. P. Bunger et al. (2013) and for a constant volume in Peirce (2025). We outline these solutions here.

Starting from the governing equation (15), we assume power-law scalings $L \sim t^{\beta}$ and $\bar{w}_0 \sim t^{\gamma}$ for the fracture length and characteristic width at the source ($x = 0$). Through the local elasticity relation (12), the source pressure scales as $\bar{w} \sim p \sim t^{\gamma}$. Substituting these into (15) gives

$$\underbrace{\frac{t^{\gamma}}{t}}_{\partial\bar{w}/\partial t} \sim \underbrace{\frac{t^{4\gamma}}{t^{2\beta}}}_{\bar{w}^4/x^2}, \tag{29}$$

where the constant prefactor $\bar{E}/(4\bar{\mu}H)$ carries no time dependence and has been omitted. Equating exponents on both sides yields

$$\gamma - 1 = 4\gamma - 2\beta \quad \Longrightarrow \quad 2\beta = 3\gamma + 1. \tag{30}$$

while mass conservation for an injection history where the volume scales as $V \sim t^{\alpha}$ (corresponding to a flux $Q_0 \sim t^{\alpha-1}$) requires

$$\gamma + \beta = \alpha. \tag{31}$$

Solving these simultaneously yields the general scaling exponents

$$\gamma = \frac{2\alpha - 1}{5}, \quad \beta = \frac{3\alpha + 1}{5}. \tag{32}$$

Here α defines the boundary condition at the source: $\alpha = 0$ corresponds to a fixed volume (instantaneous release), $\alpha = 1$ to a constant flux. For constant pressure, we fix γ to zero, giving $\alpha = 1/2$ and a decaying flux, $Q_0 \sim t^{-1/2}$.

4.1.4 Comparison of propagation patterns

Table 1 shows the difference between the KGD and PKN geometries: in the KGD model, H is absent, width and length are coupled through plane-strain elasticity ($w \sim Lp/E'$). In the PKN model, the fixed height H appears explicitly in every scaling expression, and the decoupling of width from length yields power-law solutions for all three boundary conditions.

When driven by a constant pressure the KGD solution is not a power-law and the fracture accelerates. KGD plane strain elastic models can have a counter-intuitive scaling that is markedly different from the expected scaling for fixed-height 3D fractures if the source boundary condition is not carefully prescribed. We note that for this geometry, if we force the source condition to $q_0 \propto t^{-1/2}$ instead of a constant pressure condition, our scaling requires $L \propto t^{5/12}$ and the source width relation becomes $w(x = 0) \propto t^{1/12}$. If we instead fix the source width of the KGD geometry (with $\alpha = 1/3$), we find $L \propto t^{1/3}$. These results are more akin to its constant pressure PKN counterpart ($L \propto t^{1/2}$), but both scale more slowly and as for all KGD power-law solutions the source pressure decreases with time as $p_0 \propto t^{-1/3}$, meaning neither truly replicates the constant pressure condition.

Table 1 shows that PKN fractures driven laterally by a constant flux scale as $L \propto t^{4/5}$. Under constant flux within a rigid open slot, the scaling would be linear; the reduction to a 4/5 exponent reflects the elastic compliance of the fracture walls causing resistance to lateral flow. At the other end member, where a finite volume is released into the PKN geometry, the fluid thins and spreads as $L \propto t^{1/5}$. The physics here are akin

to a droplet spreading over a surface under gravity, where flow is driven by differences in the droplet height; in our system, it is driven by differences in the fracture aperture (12). The fluid speed rapidly decays in this case as gradients in the aperture decrease as the fluid spreads. Because the local elasticity relation (12) ties source pressure to source width, each condition implies a distinct source-pressure history: a constant flux requires p_0 to rise as $t^{1/5}$ as fluid accumulates faster than it flows to the tip, while a finite-volume release causes p_0 to fall as $t^{-1/5}$, steeply at first then more gradually, as the fixed batch spreads and thins.

Note the similarity of these PKN results to those provided by Lister and Kerr (1991, sec.5.4) for a lateral dyke trapped at a density/stress step with a varying height. While Lister's results assume local cross-sectional elasticity and utilise a different cross-sectional profile, they yield a conceptually similar set of power-law scalings for all three boundary conditions: $L \propto t^{16/22}$ for a constant flux, $L \propto t^{11/22}$ for a constant pressure and $L \propto t^{6/22}$ for a finite volume release. Adachi et al. (2010) show that, for a pseudo-3D fracture that can vary in height but is confined by stress barriers, this follows the $L \propto t^{4/5}$ scaling predicted by a fixed-height PKN fracture driven by a constant flux. However, at late times when the vertical tips near the source break through the confining barriers, the fracture experiences unstable 'runaway' height growth. At this point, the assumptions of vertical pressure equilibrium fail, and the model loses its physical meaning. Similarly, Peruzzo and Lecampion (2026) show that when containment is provided by tougher bounding layers rather than stress barriers, the fracture adopts a confined PKN-like geometry that remains a good approximation for extended periods, but will also always ultimately break through into the upper and lower bounding layers, under continued fixed-rate injection. Note, this eventual runaway height growth, where the fracture extends into the upper and lower confining layers at late-times, only occurs under a constant flux forcing where the source width and height grow with time. Source widths and heights do not grow under a constant pressure forcing and these decay under the constant volume forcing, both of which will result in continued stable growth throughout propagation.

The numerics in Fig.5a) model a fixed-height fracture with non-local elasticity driven by a constant pressure source condition. The slope of the curve which relates to the tip velocity has already significantly departed from the KGD prediction once $L/H = 1$. During the transition between equidimensional and laterally elongated geometries, the predicted length converges to within 25% of the respective PKN analytical predictions once $L/H > 3$ and converging within 10% when $L/H > 5$ (Table 1). Fig.5 shows these trends are consistent across boundary conditions. When the numerics are compared against the analytical PKN predictions for both constant-flux (Q_0) and constant-volume (V_0) injection, the numerics converge to the PKN solution even faster. For both, once $L/H = 1$, the speed departs by no more than 10% from the analytical prediction, suggesting that PKN approximations are valid even for equidimensional laterally propagating dykes provided the source flux follows a power-law scaling at all times. The largest deviations from the PKN scaling at low L/H occur for the constant-pressure boundary condition, directly owing to the difference between the KGD and PKN scalings for pressure-driven propagation discussed in Sec. 4.1.2.

4.2 Self-similar fracture width profiles

Self-similar width profiles $\Omega(\xi)$ for each source condition follow from the scaling analysis of §4.1.1–4.1.3 by seeking solutions of the form

$$\Omega(\xi) = \frac{\bar{w}(x,t)}{\bar{w}_0(t)}, \qquad \xi = \frac{x}{L(t)}, \tag{33}$$

with $\bar{w}_0(t)$ and $L(t)$ given by the characteristic scales in Table 1. Substituting (33) into the governing PDE and mass conservation, the dimensional prefactors cancel and the

KGD, $L \ll H$				
Source condition	L	$w(x=0)$	C_L	C_w
Constant flux q_0	$C_L \left(\frac{E' q_0^3}{8\mu'}\right)^{1/6} t^{2/3}$	$C_w \left(\frac{\mu' q_0^3}{8E'}\right)^{1/6} t^{1/3}$	0.88	1.56
Constant pressure p_0	$L_0 \exp\left(C_L \frac{p_0^3}{\mu' E'^2} t\right)$	$C_w \frac{p_0}{E'} L(t)$	4.20	3.31
Finite area release A_0	$C_L \left(\frac{E' A_0^3}{8\mu'}\right)^{1/6} t^{1/6}$	$C_w \frac{A_0}{2L(t)}$	1.13	1.24
PKN, $L \gg H$				
Source condition	L	$\bar{w}(x=0)$	C_L	C_w
Constant flux Q_0	$C_L \left(\frac{\bar{E} Q_0^3}{32\bar{\mu} H^4}\right)^{1/5} t^{4/5}$	$C_w \frac{Q_0 t}{2L(t)H}$	1	1.33
Constant pressure p_0	$C_L \left(\frac{H p_0^{3/2}}{2\bar{\mu}^{1/2}\bar{E}}\right) t^{1/2}$	$C_w \frac{p_0 H}{\bar{E}}$	1.74	1
Finite volume release V_0	$C_L \left(\frac{\bar{E} V_0^3}{32\bar{\mu} H^4}\right)^{1/5} t^{1/5}$	$C_w \frac{V_0}{2L(t)H}$	1.85	1.19

Table 1. Length and width scaling laws with numerically determined leading prefactors C_L and C_w. The PKN results use average cross-sectional width $\bar{w}$ and depend on fracture height H, while the KGD results use width w where A_0 and q_0 represent the input area and flux respectively.

system reduces to a time-independent boundary-value problem for $\Omega(\xi)$ alone. This cancellation is guaranteed precisely because $\bar{w}_0$ and L were constructed to balance every term in the PDE and mass conservation simultaneously.

We extract $\Omega(\xi)$ from our numerical simulations by rescaling the computed width profiles using the characteristic scales of Table 1. Figure 6 shows the resulting profiles for all combinations of geometry and source condition. Note we have verified our PKN profiles match the closed-form series solution of D. I. Garagash (2025), which gives $\Omega(\xi)$ as a function of the injection power-law exponent α.

In all profiles in Figure 6 the fracture width decreases monotonically towards the tip. Moreover, the profiles for the different forcing conditions are surprisingly similar within each geometry, suggesting that the source condition would be difficult to distinguish from static snapshots of ground deformation alone. Comparing the individual cases more closely, the constant-pressure and constant-flux profiles are nearly indistinguishable for both geometries, while the constant-volume case produces a noticeably wider fracture with a steeper gradient near the tip. Note how the PKN fractures have wider noses as the tip is approached. The KGD self-similar geometries are used to initialise the numerical solutions in Fig.5.

5 Comparison to seismic data

Our scaling analysis predicts that the propagation speed of a lateral dyke decays as a power law whose exponent depends on the source boundary condition. We now test which scaling best fits the seismicity front deceleration observed during six lateral dyking episodes (Fig. 1).

For each intrusion in Fig.1, along-strike distance is measured from a reference point after rotating coordinates into a dyke-parallel frame; for the Reykjanes intrusions, the nucleation site is independently constrained by geodetic observations, whereas for the

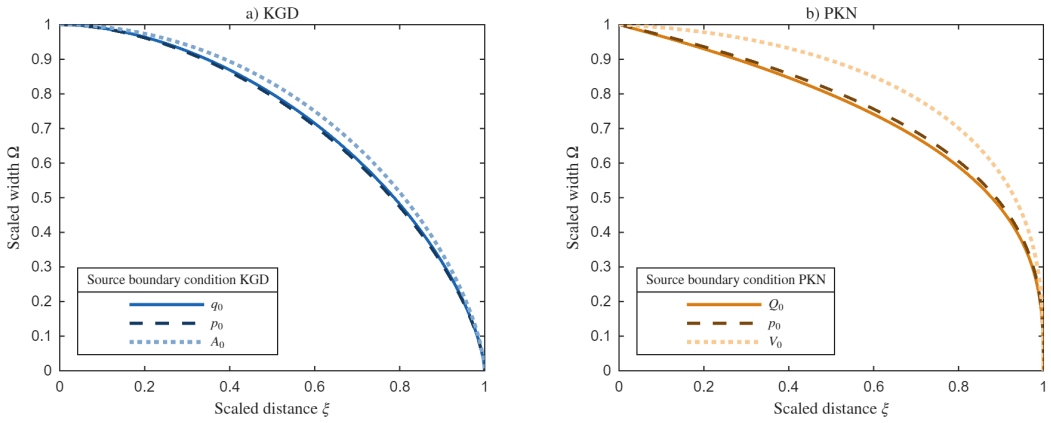

Figure 6. Self-similar width profiles of propagating fractures driven by different forcing. **Panel a** KGD fractures. **Panel b** PKN fractures.

Krafla and Afar intrusions no such constraint is available and we instead use the location of a first seismic event (Supporting Information). In Fig.7 both time and distance are normalised by the manually selected arrest time and arrest length respectively (shown as crosses on Fig.1 where the times and lengths are provided in the Supporting Information). Seismicity is filtered to events occurring after the catalogued start time and within one-third of the final dyke length perpendicular to the inferred strike direction.

For all these dykes, $L > H$, so we compare the seismicity to the reference slopes for the PKN constant flux scaling ($L \propto t^{4/5}$), PKN constant-pressure scaling ($L \propto t^{1/2}$) and the PKN finite-volume release scaling ($L \propto t^{1/5}$) using a logarithmic scale (Fig. 7). Across all six episodes, the data follow the $t^{1/2}$ scaling between scaled times of 10^{-1} and 10^{0}. At earlier times, the logarithmic scaling amplifies measurement uncertainties, producing greater scatter.

The agreement with the $t^{1/2}$ scaling shows that propagating dykes are driven by a near-constant pressure at their source, corresponding to an inlet flux that decays as $Q_0 \propto t^{-1/2}$. Two alternative source conditions can be ruled out on the basis of the data. First, the data are inconsistent with the $L \propto t^{1/5}$ scaling predicted for a finite-volume release, in which the chamber rapidly exhausts its supply resulting in a fluid batch that subsequently spreads under elastic pressure gradients alone. The absence of any transition towards this weaker scaling during propagation indicates that the dyke remains in pressure equilibrium with its source throughout. Second, a constant-flux condition is unsupported by the data. Constant-flux driving is expected when a strong topographic stress gradient acts upon a slot of constant width—which is itself established for PKN geometries by a constant source pressure (Davis et al., 2026). Under these conditions, the gradient forces a steady fluid flux through the slot. However, this mechanism does not apply to the short dykes in the relatively flat-lying settings analysed here, where topographic gradients are negligible.

The persistence of the constant-pressure scaling implies that the driving pressure at the dyke's source is sustained throughout the propagation phase. This could be achieved if the source chamber is buffered by resupply from a deeper reservoir, or if its pressure is cyclically replenished by gravitational, piston-like subsidence of the overlying roof (Roman & Lundgren, 2021). Alternatively, magma compressibility may sustain the source pressure: because the bulk magma in the source expands slightly as mass is withdrawn, the source can supply a large dyke while depressurising only a little (Rivalta & Segall, 2008). Lastly, eruption at the surface may also pin the dyke to a fixed pressure, as near-source

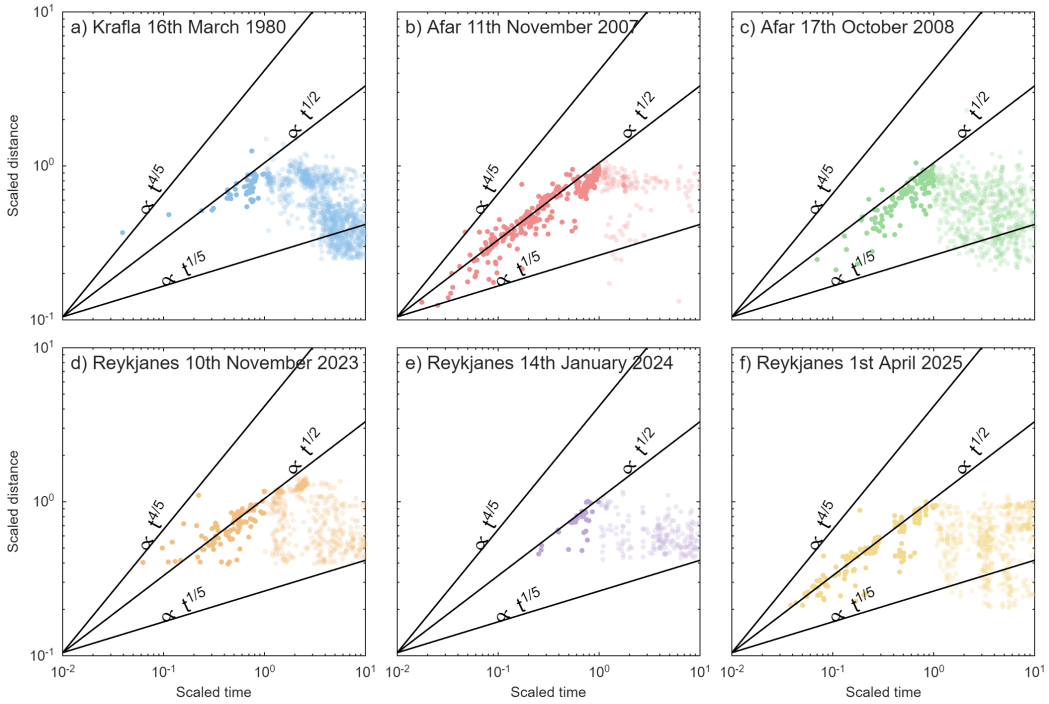

Figure 7. Spatio-temporal patterns of seismicity for different dyke intrusions scaled by arrest length and time shown as a black cross in Fig.1. Note the slight transparency of points after their arrest time.

venting prevents further pressurisation within the dyke regardless of source flux; as may be the case for dykes a) and f) in Fig.1, which broke the surface early during propagation (Supporting Information).

Geodetic inversions show decreasing rates of both dyke and source volume change (Rivalta, 2010; Sigmundsson et al., 2024). This corroborates our finding that lateral dyking is not driven by a fixed-flux. More precisely, if driven by a constant-pressure, the intruded dyke volume should grow as $V \propto t^{1/2}$. A geodetic dataset with sufficient resolution and accuracy to recover the dyke volume history during a single lateral propagation episode would provide a direct test of this scaling, independent of the seismicity-front analysis presented above.

6 Discussion

6.1 The influence of model geometry and source conditions

The scaling of dyke length with time depends on the source boundary condition and the fracture geometry. For $L/H > 3$, a fracture where the full elastic coupling is considered has a length within 25% of the analytical PKN scaling; this prediction improves further as the fracture elongates. In this limit the lubrication equation governing lateral flow becomes independent of the elastic kernel in x, and our numerical results confirm convergence above $L/H > 3$. We model a fracture symmetrical about $x = 0$, whereas many natural dykes propagate predominantly in one direction. But once the elastic kernel decouples, a one-sided dyke is simply one half of our symmetric solution, so the length scaling is unchanged.

The PKN geometry yields three distinct scaling regimes depending on the source condition. A dyke fed by a constant flux propagates as $L \propto t^{4/5}$: elastic resistance to opening reduces the speed relative to that of flow through a rigid-walled conduit. A dyke whose source width is held constant by a sustained fluid pressure gives $L \propto t^{1/2}$. A finite volume release, where stored fluid spreads laterally under elastic restoring pressures, gives $L \propto t^{1/5}$ and therefore decelerates rapidly. These results are similar to those of Lister and Kerr (1991, sec.5.4) for a dyke trapped at a density or stress step that is free to vary in height but propagates laterally under locally plane-strain elasticity; they obtain $L \propto t^{16/22}$, $L \propto t^{11/22}$ and $L \propto t^{6/22}$ for the constant flux, constant pressure and finite volume conditions respectively. The close agreement despite the different treatment of vertical extent suggests that the fixed-height assumption captures the first-order behaviour of lateral propagation.

We also neglect the vertical effect of the free surface, and it too makes little difference. Davis et al. (2026, Supplementary material sec.2b) model dyke cross-sections trapped at the level of neutral buoyancy and find that breaching the free surface reduces the cross-sectional pressure–width relation by only around 25%, with negligible change for dykes that approach but do not intersect the surface. Since lateral propagation is set by this pressure–width relation, which is barely affected by the dyke's proximity to the free surface, the free surface should not exert a first-order influence on the propagation speed or width evolution of dykes.

A dyke driven by a constant pressure has early exponential growth as predicted by the KGD solution, but this KGD prediction becomes inaccurate at L/H ratios above one (Fig.5). Two consequences follow. First, 2D plane-strain models of coupled flow and elasticity during lateral dyke propagation are unlikely to provide accurate results, since the plane-strain limit is not reached even for dykes as short as their height (Grossman-Ponemon et al., 2020; Blackstone et al., 2024). Second, under constant-pressure forcing the plane-strain and PKN scalings differ fundamentally: the former predicts exponential growth $L \propto \exp(t)$ rather than a power law, producing an acceleration that is not corroborated by the data. The constant-flux and finite-volume plane-strain scalings, by contrast, remain comparable to their PKN equivalents suggesting that plane strain models can work under these conditions.

6.2 The influence of additional processes

This study provides simple scaling laws for lateral dyke propagation using methods from the hydraulic fracturing literature. The model is three-dimensional and couples fluid flow with elasticity, but adopts a deliberately simple geometry to isolate the leading-order controls on propagation speed. Several processes omitted from the model have been studied in detail in the hydraulic fracturing literature, and we briefly assess their likely influence here.

6.2.1 Fracture tip mechanics

A possible concern for the scalings derived above is the presence of a low-pressure, vapour-filled cavity, or lag, ahead of the magma front, arising when viscous flow into the tapering tip cannot keep pace with crack opening (Lister, 1990; Rubin, 1993). For the deep, laterally extensive dykes considered here (Fig.1), lag length can be estimated from hydraulic-fracturing theory and is vanishingly small relative to the dyke length (Lister, 1990; D. Garagash & Detournay, 2000). Even were it not, the asymptotic structure near the tip shields the main body of the fracture from conditions within the lag region, leaving the length and width scalings unaffected (Detournay, 2004). Field evidence for a vapour-filled tip during propagation is correspondingly limited; altered tip zones reported in some studies (e.g., Hoek, 1994) are difficult to distinguish from post-emplacement modification such as rock fluidisation, which models suggest occurs only after arrest (Köpping et al., 2024).

The scaling relations derived in Section 4 assume that viscous dissipation dominates the energy budget of the propagating fracture, but in reality, energy is also expended in fracturing rock at the tip, characterised by the fracture toughness K_c. Toughness has been measured on the order of MPa$\times$m$^{1/2}$ for Icelandic basalts at relevant pressures and temperatures (Balme et al., 2004). Does this mean it is a dominant energy sink? Recasting the governing equations in dimensionless form (Supporting Information) collapses the competition onto a single parameter $\mathcal{K}_m^{\mathrm{PKN}}$ comparing toughness to viscous dissipation. When $\mathcal{K}_m^{\mathrm{PKN}} \ll 1$ the fracture is in a viscosity dominated regime. For the well-constrained 2024 Svartsengi intrusion (Sigmundsson et al., 2024) we estimate this parameter is around 0.06, placing the dyke firmly in the viscous regime. Whether a fracture transitions toward a toughness dominated regime is set by the supply history at the source, not by the rock or magma rheology. $\mathcal{K}_m^{\mathrm{PKN}} \propto t^{(1-2\alpha)/5}$ so for a constant-flux source ($\alpha = 1$) this pushes the dyke deeper into viscous control; constant-pressure sources ($\alpha = 1/2$) hold the balance fixed. A finite-volume release ($\alpha = 0$) reaches toughness only on timescales far exceeding any real propagation length. Toughness is therefore negligible for the laterally extensive dykes considered here, justifying the viscosity-dominated scaling.

6.2.2 Fluid rheology

Our model considers a fracture filled with a Newtonian incompressible magma where flow is laminar. In reality magma is multiphase, containing bubbles and crystals, so may be compressible and shear thinning (Rivalta & Segall, 2008; Kavanagh et al., 2025; Huber et al., 2025). In addition, magma may flow at rates where inertial forces overcome viscous resistance, exceeding the critical Reynolds number and resulting in turbulent flow. Some dykes exhibit lateral fluxes consistent with turbulent fluid flow (e.g. Sigmundsson et al., 2024). Here we demonstrate that these effects are unlikely to significantly affect the scaling of power laws for front deceleration that depend on source condition.

Magma compressibility, neglected in our model, links the internal fluid pressure to the fractional density change via the mass balance $\Delta\rho/\rho_0 = \beta_m p$, where β_m is the magma compressibility and p the net pressure (Rivalta & Segall, 2008). For KGD viscosity-dominated growth, p_0 scales as $(E'^2\mu'/t)^{1/3}$ (Detournay, 2004), giving p_0 of order a few MPa for typical basaltic dykes. For p_0 of a few MPa and $\beta_m \approx 10^{-10}$ Pa^{-1} for basaltic magma as in Rivalta and Segall (2008), $\beta_m p_0 \sim 10^{-4}$ meaning the fractional density change is very small. For comparison, Wang et al. (2018) simulated KGD viscosity-dominated fractures driven by a constant flux of supercritical CO_2 where $\beta_m p_0 \sim 1$ and found that fracture length, width and pressure were perturbed by no more than a few percent. This is corroborated by experiment and theory: radial foam-driven fractures recover the incompressible scaling even for density changes of order 10% (Lai et al., 2018; Zheng, 2026). The present problem has $\beta_m p_0$ orders of magnitude lower, showing compressibility can

be neglected for the propagation dynamics of basaltic dykes. However, compressibility remains important, for the volume budget between the dyke and its source, where the relevant ratio is β_m/β_c rather than $\beta_m p_0$, and can be of order unity even when compressibility is negligible for propagation (Rivalta & Segall, 2008).

Bubble rich magmas can show shear thinning behaviour (Rust & Manga, 2002; Kavanagh et al., 2025). Dontsov (2022) has shown that a shear-thinning power-law fluid in a constant-flux PKN fracture modifies the length scaling only mildly, from $L \propto t^{4/5}$ to $L \propto t^{3/4}$, a smaller effect than the choice of source boundary condition. Also note that a shear-thinning fluid rheology does not influence the toughness-dominated solution. Zia and Lecampion (2017) find that including turbulent flow in a height-contained, constant-flux fracture changes the length–time exponent by only around 2%. These results suggest that compressibility, non-Newtonian rheology or turbulence would not substantially alter our scaling predictions.

7 Conclusions

We derived scaling laws for the length, width, and shape of lateral dykes under different forcing. We considered three source boundary conditions and two end-member fracture geometries. For the PKN (laterally elongated) geometry, these yield distinct power-law scalings: $L \propto t^{4/5}$ for constant flux, $L \propto t^{1/2}$ for constant pressure, and $L \propto t^{1/5}$ for a finite volume release. Using a 3D elastic integral to model intermediate length-to-height ratios, we showed that the PKN scaling is accurate once L/H exceeds around three. The KGD scalings for constant flux and finite volume are comparable to their PKN counterparts, but the constant-pressure case is fundamentally different, producing exponential growth in length rather than a power law. This arises from a positive feedback between crack opening and lengthening that is absent when the fracture height provides an independent elastic length scale. Two-dimensional plane-strain models of lateral dyke propagation must therefore prescribe the flux history carefully to avoid this unphysical behaviour; imposing $q \propto t^{-1/2}$ or fixing the source width recover slower scalings than the PKN constant-pressure result but do not reproduce the constant source pressure condition itself. Self-similar width profiles show that the propagating dyke shape is nearly indistinguishable across source conditions, particularly between constant flux and constant pressure in the PKN geometry. This implies that the source driving mechanism cannot be identified from a single geodetic snapshot of dyke opening.

Comparing our scaling predictions to seismicity from six lateral dyking episodes with $L < 25$ km we find that the data consistently follow $L \propto t^{1/2}$, the scaling predicted when the magma source maintains pressure equilibrium with the growing dyke. This rules out both a constant-flux source, which would require the chamber to force magma without feedback from dyke pressure, and a finite-volume release, in which the source disconnects early. The persistence of constant-pressure scaling implies that the dyke remains coupled to a sustained source pressure, potentially through: resupply from depth buffering the chamber, magma compressibility offsetting volume loss during withdrawal, gravitational roof collapse maintaining steady pressure, or near-source surface venting that pins the dyke to a fixed pressure. A well-constrained source condition is a prerequisite for any model that probes the dynamics of dyke intrusions, including the mechanisms of arrest and start-stop behaviour. Having established that the source maintains a near constant pressure, the natural next step is to test the ability of this framework to forecast the temporal evolution of dykes.

Open Research Section

Seismicity catalogues and the MATLAB code used to model fixed-height lateral dyking are archived at `https://doi.org/10.5281/zenodo.20530826` (Davis, 2026).

Conflict of Interest disclosure

The authors declare there are no conflicts of interest for this manuscript.

Acknowledgments

We thank Bryndís Brandsdóttir, Cynthia Ebinger, Elías Heimisson and the Icelandic Meteorological office for promptly responding and providing the seismicity data used in this manuscript.

T.D. and J.B. were supported by the NERC Centre for the Observation and Modelling of Earthquakes, Volcanoes, and Tectonics (COMET, http://comet.nerc.ac.uk). T.D. and J.B. received funding from the European Research Council (ERC) under the European Union's Horizon 2020 research and innovation programme (MAST; Grant No. 101003173).

References

Adachi, J. I., Detournay, E., & Peirce, A. P. (2010). Analysis of the classical pseudo-3D model for hydraulic fracture with equilibrium height growth across stress barriers. *International Journal of Rock Mechanics and Mining Sciences*, *47*(4), 625–639. doi: 10.1016/j.ijrmms.2010.03.008

Adachi, J. I., & Peirce, A. P. (2008). Asymptotic analysis of an elasticity equation for a finger-like hydraulic fracture. *Journal of Elasticity*, *90*(1), 43–69. doi: 10.1007/s10659-007-9122-4

Ágústsdóttir, T., Woods, J., Greenfield, T., Green, R. G., White, R. S., Winder, T., ... Soosalu, H. (2016). Strike-slip faulting during the 2014 Bardarbunga-Holuhraun dike intrusion, central Iceland. *Geophysical Research Letters*, *43*(4), 1495–1503. doi: 10.1002/2015GL067423

Balme, M., Rocchi, V., Jones, C., Sammonds, P., Meredith, P., & Boon, S. (2004). Fracture toughness measurements on igneous rocks using a high-pressure, high-temperature rock fracture mechanics cell. *Journal of Volcanology and Geothermal Research*, *132*(2-3), 159–172.

Bato, M., Lundgren, P., Pinel, V., Solidum Jr, R., Daag, A., & Cahulogan, M. (2021). The 2020 eruption and large lateral dike emplacement at Taal volcano, Philippines: Insights from satellite radar data. *Geophysical Research Letters*, *48*(7), e2021GL092803. doi: 10.1029/2021GL092803

Belachew, M., Ebinger, C., Coté, D., Keir, D., Rowland, J., Hammond, J. O., & Ayele, A. (2011). Comparison of dike intrusions in an incipient seafloor-spreading segment in Afar, Ethiopia: Seismicity perspectives. *Journal of Geophysical Research: Solid Earth*, *116*(B6). doi: 10.1029/2010JB007908

Blackstone, L. A., Grossman-Ponemon, B. E., Heimisson, E. R., Lew, A. J., & Segall, P. (2024). Modeling dike trajectories in a biaxial stress field with coupled magma flow, fracture, and elasticity. *Bulletin of Volcanology*, *86*(5), 52. doi: 10.1007/s00445-024-01734-8

Bolchover, P., & Lister, J. R. (1999). The effect of solidification on fluid–driven fracture, with application to bladed dykes. *Proceedings of the Royal Society of London. Series A: Mathematical, Physical and Engineering Sciences*, *455*(1987), 2389–2409. doi: 10.1098/rspa.1999.0409

Brandsdóttir, B., & Einarsson, P. (1979). Seismic activity associated with the September 1977 deflation of the Krafla central volcano in northeastern Iceland. *Journal of Volcanology and Geothermal Research*, *6*(3-4), 197–212. doi: 10.1016/0377-0273(79)90001-5

Bunger, A., Detournay, E., Garagash, D., Clarkson, U., & Peirce, A. (2007). Numerical simulation of hydraulic fracturing in the viscosity dominated regime. In *Spe hydraulic fracturing technology conference and exhibition* (pp. SPE–

106115). doi: 10.2118/106115-MS

Bunger, A. P., Menand, T., Cruden, A., Zhang, X., & Halls, H. (2013). Analytical predictions for a natural spacing within dyke swarms. *Earth and Planetary Science Letters*, *375*, 270–279. doi: 10.1016/j.epsl.2013.05.044

Davis, T. (2026, June). *Seismicity shows lateral dyke propagation is controlled by source-dyke pressure equilibrium: Matlab code.* Zenodo. Retrieved from `https://doi.org/10.5281/zenodo.20530826` doi: 10.5281/zenodo.20530826

Davis, T., Li, Y., Pusok, A., & Katz, R. (2026). Megadyke propagation down dynamic topography. *Royal Society Proceedings A*. doi: 10.1098/rspa.2025-0733

Detournay, E. (2004). Propagation regimes of fluid-driven fractures in impermeable rocks. *International Journal of Geomechanics*, *4*(1), 35–45. doi: 10.1061/(ASCE)1532-3641(2004)4:1(35)

Detournay, E. (2016). Mechanics of hydraulic fractures. *Annual review of fluid mechanics*, *48*, 311–339. doi: 10.1146/annurev-fluid-010814-014736

Dontsov, E. (2022). Analysis of a constant height hydraulic fracture. *Mechanics of Hydraulic Fracturing: Experiment, Model, and Monitoring*, 127–139. doi: 10.1002/9781119742487.ch11

Dontsov, E., & Peirce, A. (2016). Comparison of toughness propagation criteria for blade-like and pseudo-3D hydraulic fractures. *Engineering Fracture Mechanics*, *160*, 238–247. doi: 10.1016/j.engfracmech.2016.04.023

Einarsson, P., & Brandsdóttir, B. (2021). Seismicity of the northern volcanic zone of Iceland. *Frontiers in Earth Science*, *9*, 628967. doi: 10.3389/feart.2021.628967

EMSC. (2025). *Earthquake sequence between Santorini Amorgos islands since January the 27th 2025* (Tech. Rep.). European-Mediterranean Seismological Centre. `https://static2.emsc.eu/Special_reports/?id=351`. (Last update: 27 March 2025 at 08:56 UTC)

Garagash, D., & Detournay, E. (2000). The tip region of a fluid-driven fracture in an elastic medium. *J. Appl. Mech.*, *67*(1), 183–192. doi: 10.1115/1.321162

Garagash, D. I. (2006). Plane-strain propagation of a fluid-driven fracture during injection and shut-in: Asymptotics of large toughness. *Engineering fracture mechanics*, *73*(4), 456–481. doi: 10.1016/j.engfracmech.2005.07.012

Garagash, D. I. (2025). Propagation of elongated fluid-driven fractures: Rock toughness versus fluid viscosity. *Journal of Applied Mechanics*, *92*(6), 061009. doi: 10.1115/1.4068114

Geertsma, J., & De Klerk, F. (1969). A rapid method of predicting width and extent of hydraulically induced fractures. *Journal of petroleum technology*, *21*(12), 1571–1581. doi: 10.2118/2458-PA

Grossman-Ponemon, B. E., Heimisson, E. R., Lew, A. J., & Segall, P. (2020). Logarithmic growth of dikes from a depressurizing magma chamber. *Geophysical Research Letters*, *47*(4), e2019GL086230. doi: 10.1029/2019GL086230

Heimisson, E. R., & Segall, P. (2020). Physically consistent modeling of dike-induced deformation and seismicity: Application to the 2014 Bardarbunga dike, Iceland. *Journal of Geophysical Research: Solid Earth*, *125*(2), e2019JB018141. doi: 10.1029/2019JB018141

Hoek, J. D. (1994). *Mafic dykes of the Vestfold Hills, East Antarctica: An analysis of the emplacement mechanism of tholeiitic dyke swarms and of the role of dyke emplacement during crustal extension* (PhD thesis). Utrecht University, Utrecht, Netherlands. (CIP-Data Koninklijke Bibliotheek, Den Haag. ISBN: 90-9007669-7. With summary in Dutch)

Huber, C., Bachmann, O., Florez, D., Parmentier, E., Peč, M., Latt, J., ... Das, U. (2025). The mechanics of multiphase magmas: A perspective from the scale of crystals and bubbles to magma reservoirs. *Annual Review of Earth and Planetary Sciences*, *54*. doi: 10.1146/annurev-earth-032524-124419

Isken, M. P., Karstens, J., Nomikou, P., Parks, M. M., Drouin, V., Rivalta, E., ... others (2025). Volcanic crisis reveals coupled magma system at Santorini and Kolumbo. *Nature*, *645*(8082), 939–945. doi: 10.1038/s41586-025-09525-7

Kavanagh, J. L., Chalk, C. M., Jones, T. J., & Dennis, D. J. (2025). The hidden internal flow dynamics of shear-thinning magma in dikes. *AGU Advances*, *6*(2), e2024AV001495. doi: 10.1029/2024AV001495

Kemp, L. F. (1990). Study of Nordgren's equation of hydraulic fracturing. *SPE Production Engineering*, *5*(03), 311–314. doi: 10.2118/18959-PA

Khristianovic, S., & Zheltov, Y. P. (1955). Formation of vertical fractures by means of highly viscous liquid. In *World petroleum congress proceedings* (pp. 579–586).

Köpping, J., Cruden, A. R., Thiele, S. T., Magee, C., & Bunger, A. (2024). Intrusion tip velocity controls the emplacement mechanism of sheet intrusions. *Geology*, *52*(2), 110–114.

Kovalyshen, Y., & Detournay, E. (2010). A reexamination of the classical PKN model of hydraulic fracture. *Transport in porous media*, *81*(2), 317–339. doi: 10.1007/s11242-009-9403-4

Lai, C.-Y., Rallabandi, B., Perazzo, A., Zheng, Z., Smiddy, S. E., & Stone, H. A. (2018). Foam-driven fracture. *Proceedings of the National Academy of Sciences*, *115*(32), 8082–8086. doi: 10.1073/pnas.1808068115

Lengliné, O., Duputel, Z., & Okubo, P. (2021). Tracking dike propagation leading to the 2018 Kīlauea eruption. *Earth and Planetary Science Letters*, *553*, 116653. doi: 10.1016/j.epsl.2020.116653

Lewi, E., Biggs, J., Ayele, A., Wright, T., Pagli, C., Keir, D., ... others (2025). Scientific response to the 2024–2025 dyke intrusions in the Fentale-Dofen region, Ethiopia: geophysical monitoring, surface manifestations, and hazard mapping. *Bulletin of Volcanology*, *87*(8), 64. doi: 10.1007/s00445-025-01852-x

Lister, J. R. (1990). Buoyancy-driven fluid fracture: the effects of material toughness and of low-viscosity precursors. *Journal of Fluid Mechanics*, *210*, 263–280. doi: 10.1017/S0022112090001288

Lister, J. R., & Kerr, R. C. (1991). Fluid-mechanical models of crack propagation and their application to magma transport in dykes. *Journal of Geophysical Research: Solid Earth*, *96*(B6), 10049–10077. doi: 10.1029/91JB00600

Lomax, A., Anagnostou, V., Karakostas, V., Hicks, S. P., & Papadimitriou, E. (2025). The 2025 Santorini unrest unveiled: Rebounding magmatic dike intrusion with triggered seismicity. *Science*, *390*(6775), eadz8538. doi: 10.1126/science.adz8538

Möri, A., Garagash, D., & Lecampion, B. (2023). Transition from vertical to lateral diking at the neutral buoyancy line. In *European geosciences union, annual meeting 2023 (egu2023).* doi: 10.5194/egusphere-egu23-15623

Nordgren, R. (1972). Propagation of a vertical hydraulic fracture. *Society of petroleum engineers journal*, *12*(04), 306–314. doi: 10.2118/3009-PA

OCHA. (2020). *Philippines Situation Report - Flash Update No. 3: Taal Volcano Eruption* (Tech. Rep.). United Nations Office for the Coordination of Humanitarian Affair. Retrieved from `https://www.unocha.org/publications/report/philippines/philippines-situation-report-24-jan-2020`

OCHA. (2021). *Dr congo: Volcanic eruption in goma - situation report no. #4* (Tech. Rep.). United Nations Office for the Coordination of Humanitarian Affair. Retrieved from `https://www.unocha.org/publications/report/democratic-republic-congo/dr-congo-volcanic-eruption-goma-situation-report-no-4-28-may-2021`

Peirce, A. (2025). The arrest and recession dynamics of a deflating rectangular hydraulic fracture in a permeable elastic medium. *Journal of Fluid Mechanics*, *1017*, A42. doi: 10.1017/jfm.2025.10473

Peirce, A., & Detournay, E. (2008). An implicit level set method for modeling hy-

draulically driven fractures. *Computer Methods in Applied Mechanics and Engineering*, *197*(33-40), 2858–2885. doi: 10.1016/j.cma.2008.01.013

Peirce, A., & Detournay, E. (2022). Sunset similarity solution for a receding hydraulic fracture. *Journal of Fluid Mechanics*, *944*, A7. doi: 10.1017/jfm.2022.430

Perkins, T., & Kern, L. (1961, 09). Widths of hydraulic fractures. *Journal of Petroleum Technology*, *13*(09), 937-949. Retrieved from `https://doi.org/10.2118/89-PA` doi: 10.2118/89-PA

Peruzzo, C., & Lecampion, B. (2026). Duration of hydraulic fracture containment by tougher bounding layers. *Engineering Fracture Mechanics*, 112144. doi: 10.1016/j.engfracmech.2026.112144

Rivalta, E. (2010). Evidence that coupling to magma chambers controls the volume history and velocity of laterally propagating intrusions. *Journal of Geophysical Research: Solid Earth*, *115*(B7). doi: 10.1029/2009JB006922

Rivalta, E., & Segall, P. (2008). Magma compressibility and the missing source for some dike intrusions. *Geophysical Research Letters*, *35*(4). doi: 10.1029/2007GL032521

Rivalta, E., Taisne, B., Bunger, A. P., & Katz, R. F. (2015). A review of mechanical models of dike propagation: Schools of thought, results and future directions. *Tectonophysics*, *638*, 1–42. doi: 10.1016/j.tecto.2014.10.003

Roman, A., & Lundgren, P. (2021). Dynamics of large effusive eruptions driven by caldera collapse. *Nature*, *592*(7854), 392–396. doi: 10.1038/s41586-021-03414-5

Rubin, A. M. (1993). Tensile fracture of rock at high confining pressure: implications for dike propagation. *Journal of Geophysical Research: Solid Earth*, *98*(B9), 15919–15935. doi: 10.1029/93JB01391

Rust, A., & Manga, M. (2002). Effects of bubble deformation on the viscosity of dilute suspensions. *Journal of non-newtonian fluid mechanics*, *104*(1), 53–63. doi: 10.1016/S0377-0257(02)00013-7

Sigmundsson, F., Parks, M., Geirsson, H., Hooper, A., Drouin, V., Vogfjörd, K. S., ... others (2024). Fracturing and tectonic stress drive ultrarapid magma flow into dikes. *Science*, *383*(6688), 1228–1235. doi: 10.1126/science.adn2838

Smittarello, D., Smets, B., Barrière, J., Michellier, C., Oth, A., Shreve, T., ... others (2022). Precursor-free eruption triggered by edifice rupture at Nyiragongo volcano. *Nature*, *609*(7925), 83–88. doi: 10.1038/s41586-022-05047-8

Wang, D., Chen, M., Jin, Y., & Bunger, A. P. (2018). Impact of fluid compressibility for plane strain hydraulic fractures. *Computers and Geotechnics*, *97*, 20–26. doi: 10.1016/j.compgeo.2017.12.009

Zheng, Z. (2026). A theory for foam-driven fracturing. *Journal of fluid mechanics*, *1036*, 1–30. doi: 10.1017/jfm.2026.11619

Zia, H., & Lecampion, B. (2017). Propagation of a height contained hydraulic fracture in turbulent flow regimes. *International Journal of Solids and Structures*, *110*, 265–278. doi: 10.1016/j.ijsolstr.2016.12.029

Zia, H., & Lecampion, B. (2020). Pyfrac: A planar 3D hydraulic fracture simulator. *Computer Physics Communications*, *255*, 107368. doi: 10.1016/j.cpc.2020.107368

Supporting Information for "Constraints on magma source conditions from hydraulic fracture models and seismic observations of dyke tip deceleration"

Timothy Davis[1], and Juliet Biggs[1].

[1]University of Bristol

Contents of this file

1. Text S1
2. Tables S1 to S2

Introduction This file provides the transition regimes from viscosity (M) to toughness (K) dominated fixed-height fractures. It also provides more information on the six dykes analysed in the study.

Text S1.

1. Effect of Fracture Toughness

In this section we explore the dominant energy sink during propagation, viscosity (M regime) or toughness (K regime). When toughness dominates, the pressure is nearly uniform along the fracture. For a KGD fracture where pressure has equilibrated, the shape is that of a plane strain crack subject to a constant pressure (Griffith, 1921), whereas for a PKN fracture a constant pressure condition results in a width profile that is constant from source to tip (Dontsov, 2022). We note here that if the fracture is propagating in a toughness regime, it does not necessarily arrest, for example a fracture driven by a

constant flux will continue to grow indefinitely. Arrest will occur when the mode one stress intensity is below the fracture toughness, i.e. $K_I < K_c$.

1.1. KGD

The balance between toughness and viscosity for a plane-strain fracture can be quantified through a dimensionless toughness parameter. Following Hu and Garagash (2010), the plane-strain governing equations yield a dimensionless toughness that, for a time-varying flux $q_0(t) \propto t^{\alpha-1}$, is

$$\mathcal{K}_m^{\mathrm{KGD}}(t) = \left(\frac{t}{t_*}\right)^{(1-\alpha)/4}, \qquad t_* = \frac{K'^4}{E'^3 \mu' \hat{q}_0}, \tag{1}$$

where the exponent $(1-\alpha)/4$ controls the regime evolution. When $\mathcal{K}_m \gg 1$ the toughness propagation condition controls the fracture: the pressure is nearly uniform and when $\mathcal{K}_m \ll 1$ viscous pressure gradients dominate and our viscosity dominated scaling applies.

For a constant injection rate ($\alpha = 1$), the exponent vanishes and $\mathcal{K}_m^{\mathrm{KGD}}$ is time-independent: the partitioning between viscous and toughness dissipation is fixed by the material properties and injection rate alone (Hu & Garagash, 2010). For a decaying flux or finite area release ($\alpha < 1$), $\mathcal{K}_m^{\mathrm{KGD}}$ grows with time and the fracture moves toward toughness dominance. For the constant-pressure KGD case, substituting the exponential length solution into $\mathcal{K}_m = K_c/(p_0\sqrt{L(t)})$ gives $\mathcal{K}_m \propto \exp(-t)$, confirming the fracture rapidly tends to viscous dominance. The results are summarised in Table S1.

1.2. PKN

Following Dontsov (2022) and Peirce (2025), the balance between toughness and viscosity for a PKN fracture can be quantified by non-dimensionalising the governing equations. The toughness enters through a propagation condition at the lateral fracture tip:

equating the elastic energy release rate (computed assuming plane strain in each vertical cross-section) to the fracture energy $G_c = K_c^2/E'$ yields a characteristic pressure at the tip $p(L) = \bar{K}/\sqrt{H}$ (Sarvaramini & Garagash, 2015; Dontsov & Peirce, 2016).

For a general power-law injection history with flux $Q_0(t) = \hat{Q}_0 t^{\alpha-1}$ and volume scaling $V \sim \hat{Q}_0 t^{\alpha}$, introducing dimensionless variables $\bar{w} = \bar{w}_* \Omega$, $x = L_* \xi$, $t = t_* \tau$, and $p = p_* \Pi$ into the governing equations yields four dimensionless groups (Peirce, 2025): the global volume balance, in which the fracture volume scales as $\bar{w}_* L_* H$ and the injected volume as $\hat{Q}_0 t_*^{\alpha}$, gives $\mathcal{G}_s$; the source flux condition gives $\mathcal{G}_m$; the local elasticity gives $\mathcal{G}_e$; and the toughness propagation condition gives $\mathcal{G}_k$:

$$\mathcal{G}_s = \frac{\bar{w}_* L_* H}{\hat{Q}_0 t_*^{\alpha}}, \quad \mathcal{G}_m = \frac{L_* \bar{\mu} \hat{Q}_0 t_*^{\alpha-1}}{\bar{w}_*^3 p_* H}, \quad \mathcal{G}_e = \frac{\bar{E} \bar{w}_*}{H p_*}, \quad \mathcal{G}_k = \frac{\bar{K}}{\sqrt{H}\, p_*}. \tag{2}$$

Setting $\mathcal{G}_s = \mathcal{G}_m = \mathcal{G}_e = 1$ defines the viscosity-storage (M) scaling, fixing $\bar{w}_*$, L_*, and p_* in terms of t_* with the exponents we derived: $\bar{w}_* \propto t_*^{(2\alpha-1)/5}$, $L_* \propto t_*^{(3\alpha+1)/5}$, and $p_* \propto t_*^{(2\alpha-1)/5}$, recovering our scalings for each choice of α. The remaining free group $\mathcal{G}_k$ becomes the dimensionless toughness

$$\mathcal{K}_m^{\mathrm{PKN}}(t) = \left(\frac{t}{t_*}\right)^{(1-2\alpha)/5}, \qquad t_* = \frac{\bar{K}^5 H^{7/2}}{\bar{E}^4 \bar{\mu} \hat{Q}_0^2}. \tag{3}$$

Whether the fracture transitions between regimes is therefore controlled by the source boundary condition via α. For constant flux ($\alpha = 1$), $\mathcal{K}_m \propto t^{-1/5}$, driving a $K \to M$ transition. For constant pressure ($\alpha = 1/2$), the exponent vanishes and $\mathcal{K}_m$ is time-independent: the partitioning between viscous and toughness dissipation is set entirely by the material properties and injection rate, and remains stationary throughout propagation. For a finite volume release ($\alpha = 0$), $\mathcal{K}_m \propto t^{1/5}$, driving an $M \to K$ transition. When $\mathcal{K}_m \gg 1$ the toughness propagation condition controls the fracture: the pressure is nearly

uniform and the width profile is flat from source to tip, with the length scaling linearly with time (Dontsov, 2022). When $\mathcal{K}_m \ll 1$ viscous pressure gradients dominate and our viscosity dominated scaling applies. The results are summarised in Table S1.

1.3. Application to dyke propagation models

Comparing the results in Table S1 reveals that the two geometries respond quite differently to the same source conditions. In the KGD model, constant flux is stationaryand finite area drives a fast $M \rightarrow K$ transition. In the PKN model, constant flux drives a $K \rightarrow M$ transition, constant pressure is stationary, and finite volume drives $M \rightarrow K$. The general trend can be understood from the exponent $(1-\alpha)/4$ for KGD versus $(1-2\alpha)/5$ for PKN.

Ultimately, these two models are not just alternatives but temporal stages: as a fracture lengthens ($L \gg H$), it transitions from the plane-strain KGD limit into the confined-height PKN geometry. Because the tapered aperture of the PKN cross-section forces higher viscous dissipation, this geometric evolution acts to stabilise and move the system's energy balance closer to the viscous (M) regime.

Under constant flux, the fracture moves from a stationary KGD state into the $K \rightarrow M$ transition characteristic of PKN. In the constant pressure case, viscous dominance in the KGD geometry occurs rapidly, and the transition to PKN preserves this as a stationary $\mathcal{K}_m$ regime. This results in a fracture remaining viscosity-dominated throughout propagation. Even for finite volume releases, the shift to PKN slows the approach to toughness dominance. In every scenario, as the fracture lengthens and assumes its final linguine like shape, the physics inherently favours the viscous energy sink more than the initial stage did.

To illustrate the timescales over which these processes dominate, we substitute real-world values. We use $H \sim 3$ km, $Q_0 \sim 7400$ m^3 s^{-1}, $\mu \sim 30$ Pa s and $E = 25$ GPa based on the well-constrained 2024 Svartsengi dyke intrusion (Sigmundsson et al., 2024). High pressure–temperature measurements of Icelandic basalt estimate a toughness of $K_c \sim 2.5$ MPa m$^{1/2}$ (Balme et al., 2004). For the PKN case we find $\mathcal{K}_m^{\mathrm{PKN}} = 0.06$ for a constant flux (evaluated at $t = 1$ s). Since $\mathcal{K}_m \propto t^{-1/5}$, this value only decreases with time, confirming that the fracture is firmly in the viscosity-dominated regime from the onset of propagation. For a constant-pressure source, $\mathcal{K}_m$ is time-independent (Table S1) and takes a comparable value, so the fracture remains viscosity-dominated throughout. Even in the finite-volume case, where $\mathcal{K}_m \propto t^{1/5}$ grows toward toughness dominance, the transition time far exceeds any physically relevant propagation time if we use the final dyke volume inferred from geodetic measurements $\sim 10^8$ m^3 (Sigmundsson et al., 2024). Toughness is therefore negligible for laterally propagating dykes under these conditions, justifying the viscosity-dominated scaling adopted throughout this work.

Text S2. The seismic data in the manuscript was provided by the following sources. Start dates and times use those reported but are adjusted to make sure the first event is close to zero time and zero distance on the graphs.

Krafla, Iceland 1980's data from Bryndís Brandsdóttir (Brandsdóttir & Einarsson, 1979) and dates and times from Einarsson and Brandsdóttir (2021).

Afar, Ethiopia 2000's data from Cynthia Ebinger (Belachew et al., 2011). Belachew et al. (2011) provide the dates and times.

Reykjanes, Iceland 2020's data from the Icelandic Meteorological Office catalog `https://`

skjalftalisa.vedur.is/#/page/map with dates and times from Parks et al. (2025).

References

Balme, M., Rocchi, V., Jones, C., Sammonds, P., Meredith, P., & Boon, S. (2004). Fracture toughness measurements on igneous rocks using a high-pressure, high-temperature rock fracture mechanics cell. *Journal of Volcanology and Geothermal Research*, *132*(2-3), 159–172.

Belachew, M., Ebinger, C., Coté, D., Keir, D., Rowland, J., Hammond, J. O., & Ayele, A. (2011). Comparison of dike intrusions in an incipient seafloor-spreading segment in Afar, Ethiopia: Seismicity perspectives. *Journal of Geophysical Research: Solid Earth*, *116*(B6). doi: 10.1029/2010JB007908

Brandsdóttir, B., & Einarsson, P. (1979). Seismic activity associated with the September 1977 deflation of the Krafla central volcano in northeastern Iceland. *Journal of Volcanology and Geothermal Research*, *6*(3-4), 197–212. doi: 10.1016/0377-0273(79)90001-5

Dontsov, E. (2022). Analysis of a constant height hydraulic fracture. *Mechanics of Hydraulic Fracturing: Experiment, Model, and Monitoring*, 127–139. doi: 10.1002/9781119742487.ch11

Dontsov, E., & Peirce, A. (2016). Comparison of toughness propagation criteria for blade-like and pseudo-3D hydraulic fractures. *Engineering Fracture Mechanics*, *160*, 238–247. doi: 10.1016/j.engfracmech.2016.04.023

Einarsson, P., & Brandsdóttir, B. (2021). Seismicity of the northern volcanic zone of Iceland. *Frontiers in Earth Science*, *9*, 628967. doi: 10.3389/feart.2021.628967

Griffith, A. A. (1921). Vi. the phenomena of rupture and flow in solids. *Philosophical transactions of the royal society of london. Series A, containing papers of a mathematical or physical character*, *221*(582-593), 163–198.

Hu, J., & Garagash, D. (2010). Plane-strain propagation of a fluid-driven crack in a permeable rock with fracture toughness. *Journal of Engineering Mechanics*, *136*(9), 1152–1166.

Parks, M., Drouin, V., Sigmundsson, F., Hjartardóttir, Á. R., Geirsson, H., Pedersen, G. B., ... others (2025). 2023–2024 inflation-deflation cycles at svartsengi and repeated dike injections and eruptions at the sundhnúkur crater row, reykjanes peninsula, iceland. *Earth and Planetary Science Letters*, *658*, 119324.

Peirce, A. (2025). The arrest and recession dynamics of a deflating rectangular hydraulic fracture in a permeable elastic medium. *Journal of Fluid Mechanics*, *1017*, A42. doi: 10.1017/jfm.2025.10473

Sarvaramini, E., & Garagash, D. I. (2015). Breakdown of a pressurized fingerlike crack in a permeable solid. *Journal of Applied mechanics*, *82*(6), 061006.

Sigmundsson, F., Parks, M., Geirsson, H., Hooper, A., Drouin, V., Vogfjörd, K. S., ... others (2024). Fracturing and tectonic stress drive ultrarapid magma flow into dikes. *Science*, *383*(6688), 1228–1235. doi: 10.1126/science.adn2838

KGD – Lasagna			
Source condition	Inlet flux $q_0(t)$	Transition parameter	Regime path
Constant flux	$q_0 \propto t^0$	$\mathcal{K}_m^{\mathrm{KGD}} = \mathrm{const}$	Stationary
Constant pressure	$q_0 \propto \exp(t)$	$\mathcal{K}_m^{\mathrm{KGD}} \propto \exp(-t)$	$K \to M$
Finite area release	$q_0 \propto t^{-1}$	$\mathcal{K}_m^{\mathrm{KGD}} \propto t^{1/4}$	$M \to K$
PKN – Linguine			
Source condition	Inlet flux $Q_0(t)$	Transition parameter	Regime path
Constant flux	$Q_0 \propto t^0$	$\mathcal{K}_m^{\mathrm{PKN}} \propto t^{-1/5}$	$K \to M$
Constant pressure	$Q_0 \propto t^{-1/2}$	$\mathcal{K}_m^{\mathrm{PKN}} = \mathrm{const}$	Stationary
Finite volume release	$Q_0 \propto t^{-1}$	$\mathcal{K}_m^{\mathrm{PKN}} \propto t^{1/5}$	$M \to K$

Table S1. Summary of regime transitions for PKN and plane-strain (KGD) fractures. In both cases, $\mathcal{K}_m \ll 1$ corresponds to viscosity dominance and $\mathcal{K}_m \gg 1$ to toughness dominance. A decreasing $\mathcal{K}_m$ drives a $K \to M$ transition, while an increasing $\mathcal{K}_m$ drives $M \to K$.

Location	Krafla	Afar	Afar	Reykjanes	Reykjanes	Reykjanes
Country	Iceland	Ethiopia	Ethiopia	Iceland	Iceland	Iceland
Date (dd/mm/yy)	16/03/1980	11/11/2007	17/10/2008	10/11/2023	14/01/2024	01/04/2025
Start time (hh:mm:ss)	16:01:09	16:34:00	06:10:04	16:55:00	02:55:00	07:05:55
Start latitude	65.7158	12.2633	12.3100	63.881	63.881	63.881
Start longitude	-16.7723	40.6700	40.6070	-22.392	-22.392	-22.392
Arrest length (km)	12.1	25	14.2	8.6	7.14	14.55
Arrest time (days)	0.26	1.82	0.376	0.23	0.185	0.52
Fissural eruption (Y/N)	Y	N	N	Y	Y	Y
Eruption time (hh:mm:ss)	16:20:00	∼	∼	21:00:00	07:57:00	09:44:00
Eruption date (dd/mm/yy)	16/03/1980	∼	∼	18/12/2023	14/01/2024	01/04/2025
Bi-directional (Y/N)	N	N	N	Y	N	Y

Table S2. Table describing the general features of the dykes we study.